Enhanced azimuthal rotation of the large-scale flow through stochastic cessations in turbulent rotating convection with large Rossby numbers

Jin-Qiang Zhong,* Hui-Min Li, and Xue-Ying Wang

Shanghai Key Laboratory of Special Artificial Microstructure Materials and Technology and School of Physics Science and Engineering, Tongji University, Shanghai 200092, China

(Received 12 November 2016; published 21 April 2017)

We present measurements of the azimuthal orientation $\theta(t)$ and thermal amplitude $\delta(t)$ of the large-scale circulation (LSC) of turbulent rotating convection within a large Rossby number range $1 \leqslant \text{Ro} \leqslant 314$. Results of $\theta(t)$ reveal persistent rotation of the LSC flow in the retrograde direction over the entire Ro range. The rotation speed ratio remains a constant of 0.13 ± 0.01 for $10 \leqslant \text{Ro} \leqslant 70$, but starts to increase with increasing Ro when $\text{Ro} > 70$. We identify the mechanism through which the mean retrograde rotation speed can be enhanced by stochastic cessations in the presence of weak Coriolis force and show that a low-dimensional stochastic model, with essential refinements to account for the effect of turbulence stress, provides accurate predictions of the observed LSC dynamics and interprets its retrograde rotation.

DOI: 10.1103/PhysRevFluids.2.044602

I. INTRODUCTION

Turbulent convection in the presence of rotation occurs in a variety of natural flows in the atmosphere and the oceans [1]. Large-scale coherent flows often exist in these geophysical fluid systems and play crucial roles in their turbulent heat and mass transport. Examples include the thermohaline circulation in the oceans [2] and the tropical atmospheric circulation (the Hadley cell) [3]. The canonical framework to study turbulent convection flow is the Rayleigh-Bénard convection (RBC) system, i.e., a horizontal fluid layer heated from below and cooled from above [4,5]. In turbulent RBC, thermal plumes that emanate from the thermal boundary layers (BLs) are organized spontaneously into a large-scale circulation (LSC) (see, e.g., [6–9]). Laboratory experiments reveal that the LSC survives under the influence of modest rotations if the ratio of the buoyancy and Coriolis forces, expressed in the Rossby number (Ro), is greater than one [10,11].

A prominent dynamical feature of the LSC in turbulent rotating RBC in cylindrical samples is the azimuthal rotation of its polar circulation plane with nearly a constant velocity [8,10–14]. Developed from the fluid momentum equations, one-dimensional theoretical models suggested that when the LSC flow rotates steadily in the azimuthal direction, the Coriolis force, which accelerates the LSC rotation, is balanced by the viscous drag from the kinetic BLs [10,13]. These models predicted a constant retrograde rotation speed ω close to the sample rotating rate Ω. The model prediction was shown to be in reasonable consistency with the experimental measurements of ω (open circle, Fig. 1) when the LSC azimuthal rotation is driven by the earth's Coriolis force with $\Omega = \Omega_E \sin\phi$ [13]. Here $\Omega_E = 7.3 \times 10^{-5}$ rad/s is the earth's rotating rate and ϕ is the latitude. Experiments [10–12,15,16] with deliberate rotations (but with $\Omega \geqslant 100\Omega_E$) reported LSC rotation speeds ω about one order of magnitude less than Ω (closed symbols, Fig. 1). Moreover, conflicting results of $\omega > \Omega$ had been reported in other experiments in the presence of the earth's rotation [14,17]. Although controversial results of the LSC rotation were obtained, these experimental studies revealed, from different perspectives, a variety of azimuthal dynamics of the LSC (such as cessations and erratic rotations) that has not been accounted for in the aforementioned one-dimensional models [10,13]. Our understanding of the fundamental dynamics of the large-scale flow in rotating turbulent convection is far from complete.

*Corresponding author: jinqiang@tongji.edu.cn

 ©2017 American Physical Society

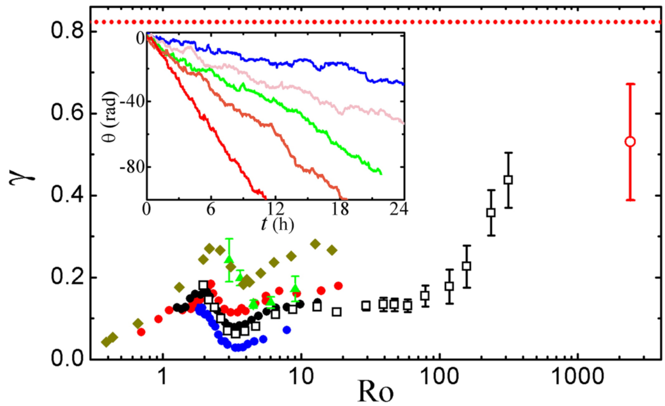

FIG. 1. Results for the LSC rotation speed ratio $\gamma = \omega/\Omega$ as a function of Ro: closed circles, data from [11] with Pr = 4.38 and Ra = 1.8×10^{10} (red), Ra = 8.97×10^{9} (black), and Ra = 2.25×10^{9} (blue); diamonds, data from [12] with Ra = 2.9×10^{11} and Pr = 8.4; triangles: data from [10] with Ra = 1.1×10^{9} and Pr = 6.37; open circle, data from [13] with Ra = 8.9×10^{10}, Pr = 4.38, and $\Omega = \Omega_E$; squares, this work; and dashed line, theoretical prediction of γ from [13] when Ra = 8.24×10^{9} and Pr = 4.38. The error bars indicate the fluctuations of ω over 24 h. The inset shows examples of $\theta(t)$ as functions of time for Ro = 13.1 (red), Ro = 18.2 (orange), Ro = 39.4 (green), Ro = 59.0 (magenta), and Ro = 236 (blue).

In this paper we present measurements of the LSC orientation $\theta(t)$ and thermal amplitude $\delta(t)$ in a large Ro range $1 \leqslant \text{Ro} \leqslant 314$. In the low-Ro range, results of the LSC rotation speed ratio γ agree well with existing experimental data. In the large-Ro range, we observe that $\dot{\theta}$ can be largely enhanced due to intense accelerations during small-amplitude events (cessations) and report an unanticipated increase of γ when Ro $\geqslant 70$. The phenomenon of cessation-enhanced azimuthal velocity has been interpreted recently by a stochastic LSC model [18–20] that describes the diffusive motion of $\theta(t)$ and $\delta(t)$. Since cessation events, normally defined by a relatively small threshold of δ_c, were commonly assumed to be rare, this model has not accounted quantitatively for the contribution of the azimuthal displacements during cessations to the long-term net rotation of the LSC. Our experimental data show that, depending on δ_c, the azimuthal displacements of cessations may play an important role in determining ω. We further elucidate that the stochastic model [18–20], with essential refinements to account for the effect of turbulence stress, can provide accurate predictions of the observed LSC dynamics and interprets its retrograde rotation.

II. EXPERIMENTAL SETUP

The experiment was performed using an apparatus described before [15,16]. We used a cylindrical sample with a height $L = 24.0$ cm and an aspect ratio of 1.00. The sample was filled with deionized water at a mean temperature of 40.00 °C. The Rayleigh number $\text{Ra} \equiv \alpha g \Delta T L^3/\kappa\nu = 8.24 \times 10^9$ and the Prandtl number $\text{Pr} \equiv \nu/\kappa = 4.38$ remained constant. Here α, ν, and κ are the thermal expansion coefficient, the viscosity, and the thermal diffusivity, respectively, and ΔT is the applied temperature difference. The bottom plate of the sample was made of oxygen-free high-conductivity (OFHC) copper (type TU1). It had a thickness of 35.0 mm and a diameter of 285.7 mm. From its bottom side a central area of 242.5 mm diameter was covered uniformly by parallel straight grooves, interconnected by semicircles at their ends. A main heater made of resistance wires was epoxied into the grooves. Seven thermistors were installed in the bottom plate, one at the center and the other six equally spaced on a circle 210.0 mm in diameter. The heater was operated in a digital feedback loop in conjunction with these thermistors to hold the bottom-plate temperature constant. Temperature inhomogeneity on the plate was less than 1% of ΔT during experiments.

The top plate was also made of OFHC copper with dimensions similar to the bottom plate. It consisted of a double-spiral water-cooling channel. To maintain a constant top-plate temperature, circulating coolant was driven into the channel by a refrigerating circulator. Although the double-spiral channels had been designed to provide a uniform temperature over the entire top plate, when coolant passed through the channel, its temperature increased slightly as it absorbed heat from the plate. A temperature difference still appeared crossing the top plate where it was coolest (warmest) near the inlet (outlet). To improve the temperature homogeneity, the coolant flow speed was first accelerated by a fluid pump up to 18 l/min before entering the channel. The entire fluid-circulation system including the circulator, the fluid pump, and the accessories was thermally isolated from the ambient temperature. The temperature stability of the circulating coolant remained at 0.01 K. With this improvement the temperature inhomogeneity over the whole top plate was reduced to about $0.01\Delta T$.

The sample had a 4-mm-thick Plexiglas sidewall. Eight thermistors, equally spaced azimuthally in the horizontal midplane of the cell, were placed in the sidewall. We measured the temperature of each thermistor T_i and fitted them with the function $T_i = T_0 + \delta\cos(i\pi/4 - \theta)$, $i = 1,\ldots,8$. Following this experimental protocol [8], we determined the LSC thermal amplitude δ and the azimuthal orientation θ of its circulating plane.

The sidewall was surrounded by a concentric thermal side shield made by 3-mm-thick aluminum. The side shield had an inner diameter of 400 mm, with a separate coolant circuit epoxied to its outer side. Thermal insulation materials (e.g., low-density foams) filled in the volume between the sidewall and the shield. When coolant from a thermal bath flowed through this circuit, the temperature of the side shield remained constant with a stability of 0.01 K. During the experiment, thermal protection towards the sidewall was provided when the side-shield temperature was kept at the mean fluid temperature of the sample.

The convection cell was mounted on a rotary table with high-quality performance for slow-rotating experiments. Before the experiment the sample was leveled by adjusting three supporting legs, using a cross-test level with a precision of 0.02 mm/m placed on the top surface of the top plate. The horizontal surfaces of the top plate and bottom plate and the Plexiglas sidewall were all finely machined; their thickness was uniform at all azimuthal orientations with an accuracy of 0.05 mm. We can thus be sure that the entire sample was leveled to better than 0.001 rad. Another set of heavy-duty leveling screws was placed at the base of the rotating table. When tuning these screws, we adjusted the rotating axis of the table to be accurately parallel to the gravity. The rotating velocity of the table Ω was selected within $(7.8 \times 10^{-4}, 0.1)$ rad/s, so $\mathrm{Ro} \equiv \sqrt{\alpha g \Delta T/L}/2\Omega$ covered the range $1 \lesssim \mathrm{Ro} \leqslant 314$ [see Appendix A for detailed information about the accuracy and stability of $\Omega(t)$].

III. RESULTS AND DISCUSSION

A. General features of the LSC azimuthal motion and its mean retrograde rotation velocity

Over the entire Ro range studied, retrograde rotation of the LSC plane was observed that led to a linear decrease of θ in time. Figure 1 shows the time series of $\theta(t)$ for several Ro. When Ro increases the mean rotating rate $\omega = |\langle\dot{\theta}\rangle|$, determined through linear fits to the traces of $\theta(t)$, decreases monotonically. The ratio of the LSC rotation speed $\gamma = \omega/\Omega$ is depicted as a function of Ro. We observe a complicated Ro dependence of γ in the range $1 \leqslant \mathrm{Ro} \lesssim 10$ that agrees with previous works [11,12]. In the range of $10 \lesssim \mathrm{Ro} \leqslant 70$, ω appears to be proportional to Ω, yielding $\gamma = 0.13 \pm 0.01$ independent of Ro. When $\mathrm{Ro} \geqslant 70$, γ gradually increases and reaches a value of 0.42 for $\mathrm{Ro} = 314$. This Ro corresponds to the slowest sample rotating rate $\Omega \approx 10\Omega_E$ we applied. The result from [13] with $\Omega = \Omega_E$ is shown by the rightmost circle.

Figure 2 shows a long time series of $\theta(t)$ for $\mathrm{Ro} = 236$. A mean retrograde rotation speed of $\omega = 0.36\Omega$ is observed in this example. We find that a broad spectrum of the LSC azimuthal dynamics contributes to the net rotation and determines ω. Over large time scales of hours $\theta(t)$

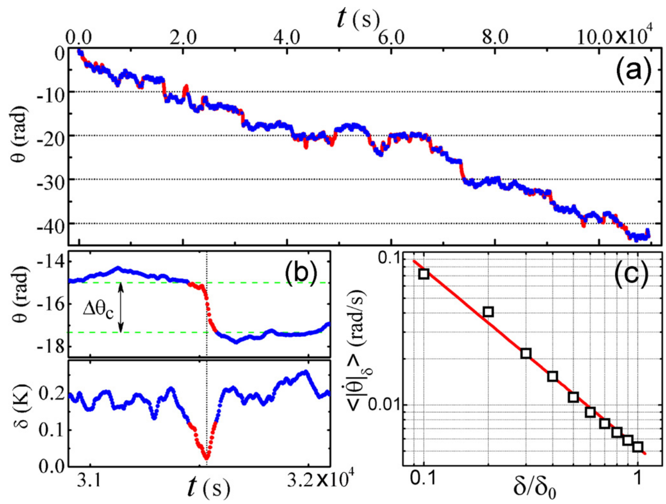

FIG. 2. (a) Long time series of $\theta(t)$ for Ro = 236. (b) Time series of both $\theta(t)$ and $\delta(t)$ during cessations. Sections in the time series with δ larger (smaller) than $\delta_c = 0.5\delta_0$ are shown in blue (red). The vertical dashed line in (b) indicates the moment when δ is minimum. (c) Conditional mean $\langle|\dot{\theta}|_\delta\rangle$ as a function of δ/δ_0. Here $\dot{\theta}$ is determined by the angular change of θ within a time interval of $dt = 4.06$ s. The straight line indicates $\langle|\dot{\theta}|_\delta\rangle = \dot{\theta}_0(\delta/\delta_0)^\beta$ with $\dot{\theta}_0 = 5.3 \times 10^{-3}$ rad/s and $\beta = -1.16$.

appears to rotate steadily at a nearly constant velocity. In a short time scale of minutes the LSC orientation undergoes meandering motion that resembles Brownian motion (see the discussion of Fig. 3). Moreover, there are occasional violent accelerations in $\theta(t)$ (shown in red) that lead to large instantaneous azimuthal velocities of up to 600 times $\langle\dot{\theta}\rangle$. These fast reorientation events occur intermittently, accompanied a decrease of the LSC amplitude δ that typifies cessation events [8] [Fig. 2(b)]. The relationship between the instantaneous azimuthal velocities $\dot{\theta}$ and δ can be quantitatively presented by the conditional expectation $\langle|\dot{\theta}|_\delta\rangle$, i.e., the time average of $\dot{\theta}$ for a given value of δ. As depicted in Fig. 2(c), $\langle|\dot{\theta}|_\delta\rangle$ increases when δ decreases and can be best represented as $\langle|\dot{\theta}|_\delta\rangle = \dot{\theta}_0(\delta/\delta_0)^{-1.16}$.

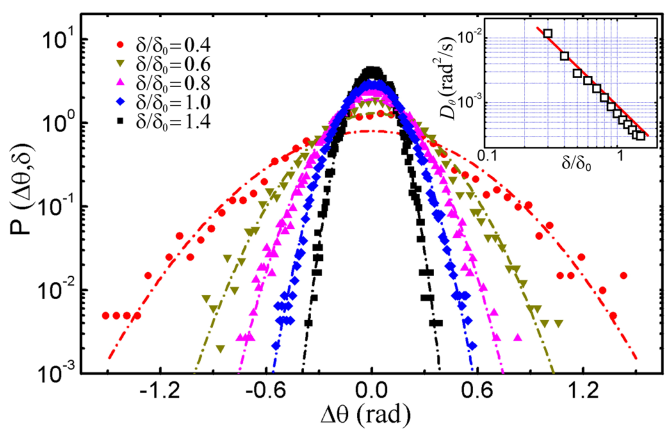

FIG. 3. Probability distribution functions (PDFs) of the azimuthal displacement $\Delta\theta$ for given amplitudes δ with Ro = 236. Dashed lines show the Gaussian fit to data. The inset shows diffusivity D_θ as a function of δ/δ_0. The solid curve shows a power function $D_\theta = D_0\delta^{-2}$ with $D_0 = 5.2 \times 10^{-5}$ rad^2 K^2/s.

B. Diffusive properties of the LSC azimuthal motion

The enhanced azimuthal rotation velocity $\dot{\theta}$ when δ is small implies that the LSC rotational inertia in its circulating plane plays an important role in determining its azimuthal rotation. To interpret this phenomenon, we develop a Langevin equation from the Navier-Stokes equation to describe the motion of $\theta(t)$ in the presence of rotations [15,16,18,20]:

$$\ddot{\theta} = -\frac{\delta}{\delta_0 \tau_{\dot{\theta}}}\dot{\theta} + \frac{\delta \Omega}{\delta_0 \tau_{\dot{\theta}}} + f_{\dot{\theta}}(t). \tag{1}$$

Here the azimuthal fluid acceleration, expressed in $\ddot{\theta}$, is given by its rotational inertia with a damping time scale $\tau_{\dot{\theta}} = L^2/2\nu\,\mathrm{Re}$ and the Coriolis force. In addition, $\delta_0 = \langle \delta \rangle$ is the mean amplitude. The background turbulent fluctuation is modeled by a δ-correlated Gaussian noise term $f_{\dot{\theta}}$, which has zero mean and an autocorrelation $\langle f_{\dot{\theta}}(t_1) f_{\dot{\theta}}(t_2)\rangle = 2\Gamma_{\dot{\theta}}\delta(t_1 - t_2)$.

Equation (1) suggests that when δ decreases, the inertial damping $\delta\dot{\theta}/\delta_0\tau_{\dot{\theta}}$ becomes smaller so the LSC plane is accelerated by the turbulent fluctuations and moves more freely in the azimuthal direction. Here we examine the angular displacement $\Delta\theta(t_s) = \tilde{\theta}(t + t_s) - \tilde{\theta}(t)$ of the detrended LSC orientation $\tilde{\theta}(t) = \theta(t) - \langle \dot{\theta} \rangle t$ and determine the conditional probability distribution $P(\Delta\theta,\delta)$ using the time series $\theta(t)$ with δ restricted to the range $(\delta - 0.1\delta_0, \delta + 0.1\delta_0)$. Figure 3 shows the results of $P(\Delta\theta,\delta)$ for several δ with a time interval $t_s = 40$ s. All of the distributions have a Gaussian shape with an increasing variance when δ decreases. They indicate that azimuthal motion of the LSC plane is well characterized by Brownian motion irrespective of the LSC amplitude δ.

Since the characteristic time scales for variations of $\theta(t)$ and $\delta(t)$ are $\tau_{\dot{\theta}} = L^2/2\nu\,\mathrm{Re}$ and $\tau_\delta = L^2/18\nu\,\mathrm{Re}^{1/2}$, respectively [18], the LSC flow strength varies slower than its azimuthal orientation ($\tau_{\dot{\theta}} \approx 10s \approx 0.1\tau_\delta$). Therefore, $P(\Delta\theta,\delta)$ reveals statistically how diffusive motion of $\theta(t)$ depends on δ [19]. Using the steady-state solution of the Fokker-Planck equation corresponding to Eq. (1), we determine

$$P(\Delta\theta,\delta) = \frac{1}{\sqrt{2\pi\sigma_\theta{}^2(t_s)}} \exp\left(-\frac{(\Delta\theta - \langle\Delta\theta\rangle)^2}{2\sigma_\theta{}^2(t_s)}\right) \tag{2}$$

with the variance [21]

$$\sigma_\theta{}^2(t_s) = 2\Gamma_\theta \tau^2 t_s + \Gamma_\theta \tau^3(-3 + 4e^{-t_s/\tau} - e^{-2t_s/\tau}) \tag{3}$$

dependent on t_s. With a sufficiently long sampling time interval $t_s \gg \tau = \tau_{\dot{\theta}}\delta_0/\delta$, we have $\sigma_\theta{}^2(t_s) = 2D_\theta t_s$, where $D_\theta = \Gamma_\theta \tau_{\dot{\theta}}^2 \delta_0^2/\delta^2$ is the diffusivity of θ.

In order to determine the diffusivity D_θ, we measure directly $\sigma_\theta{}^2(t_s) = \langle[\Delta\theta(t_s) - \langle\Delta\theta(t_s)\rangle]^2\rangle$ with the sampling time intervals t_s selected in the range $0.5\tau < t_s < 5\tau$. The two parameters Γ_θ and τ can be determined through a least-squares fit of the experimental data $\sigma_\theta{}^2(t_s)$ to Eq. (3). Following this approach, we obtain $D_\theta = \Gamma_\theta \tau^2$ as a function of δ for $0.25\delta_0 \leqslant \delta \leqslant \delta_0$. As shown in the inset in Fig. 3, $D_\theta(\delta)$ increases rapidly with decreasing δ and follows closely a simple power function $D_\theta(\delta) = D_0\delta^{-2}$. Such a power law dictates $D_\theta(\delta)$ for all Ro in the range Ro $\geqslant 5$. Hence we obtain the instantaneous azimuthal velocities due to diffusive motion for a given LSC amplitude δ, $\langle|\dot{\theta}|_\delta\rangle = \sqrt{D_\theta dt}/dt = \sqrt{\Gamma_\theta/dt}\,\tau_{\dot{\theta}}\delta_0/\delta$, which agrees with the experimental data shown in Fig. 2(c).

C. Stochastic properties of the LSC thermal amplitude

To better understand the small-amplitude behavior of the LSC, we measure the occurrence frequency f_c of cessations, which is defined to occur when $\delta < \delta_c = 0.5\delta_0$.[1] In order to ensure

[1]In viewing that a general criterion of the amplitude threshold δ_c for cessations does not exist, we choose $\delta_c = 0.5\delta_0$ in order to ensure sufficient statistics to reveal the LSC stochastic behavior under the influence of rotations. We note that the dynamical properties of cessations discussed in Fig. 4 can be well interpreted by the present model, independently of the threshold value of δ_c.

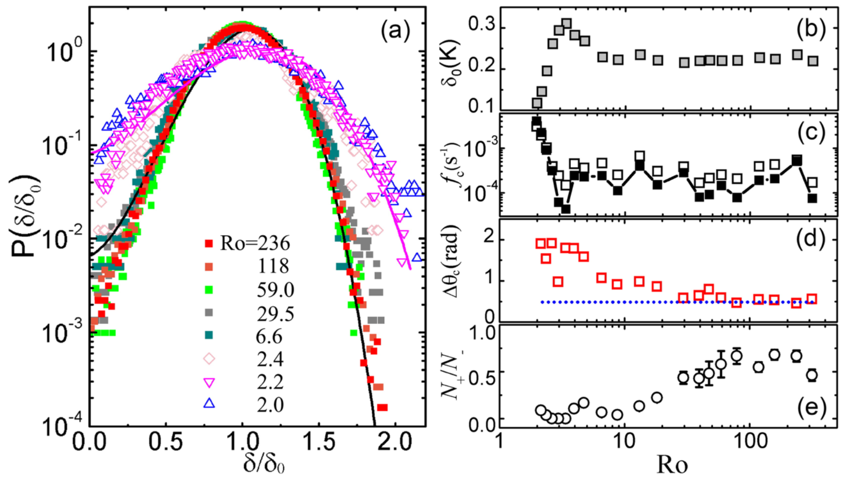

FIG. 4. Some dynamical properties of the LSC during cessations. (a) The PDFs of δ/δ_0. The two solid curves are theoretical fittings of $P(\delta/\delta_0)$ for Ro = 236 (black) and Ro = 2.2 (magenta). (b) The δ_0 as a function of Ro. (c) The f_c as a function of Ro. Open squares show experimental data and closed squares theoretical results. (d) Azimuthal displacement $\Delta\theta_c$. The dashed line shows the theoretical estimate of $\Delta\theta_d$ for Ro = 236. (e) Ratio of N_+/N_-. Error bars show the standard deviations.

sufficient statistics of f_c we record a long time series ($\sim$100 h) for each Ro in the high-Ro range. Results for f_c are depicted in Fig. 4(c). One can see that f_c remains roughly constant in the large-Ro range (Ro $\gtrsim$ 5). In the fast rotating range when Ro $\lesssim$ 5, f_c increases sharply with increasing Ω.

The dynamics of the LSC amplitude $\delta(t)$ is governed by a second Langevin equation [15,16,18,20]

$$\dot{\delta} = \frac{BD_\delta}{2\delta_0} + \frac{\delta}{\tau_\delta} - \frac{\delta^{3/2}}{\tau_\delta \delta_0^{1/2}} + f_\delta(t). \tag{4}$$

This amplitude equation, combined with Eq. (1), constitutes the full LSC model. Here the increment of the LSC strength $\dot{\delta}$ is given by the buoyancy force, the thermal diffusion, and the viscous dissipation from the BLs. In addition, $\tau_\delta = L^2/18\nu\,\mathrm{Re}^{1/2}$ is the time scale of variation in $\delta(t)$. The constant B reveals the change rate $\dot{\delta}$ when $\delta \ll \delta_0$. Further, $f_\delta(t)$ presents Gaussian noise with intensity $\Gamma_\delta = D_\delta/\tau_\delta^2$.

Equation (4) suggests that motion of $\delta(t)$ can be described in terms of diffusive motion in a potential well $V(\delta)$ [21,22]. Using the steady-state solution of the corresponding Fokker-Planck equation, we find

$$V(\delta) = -\frac{BD_\delta\delta}{2\delta_0} - \frac{\delta^2}{2\tau_\delta} + \frac{2\delta^{5/2}}{5\tau_\delta\delta_0^{1/2}}. \tag{5}$$

The probability distribution of δ/δ_0 is

$$P(\delta/\delta_0) = \frac{1}{\sqrt{2\pi}\sigma_\delta} e^{-2V(\delta/\delta_0)/D_\delta}, \tag{6}$$

with $\sigma_\delta^2 = D_\delta\tau_\delta/\delta_0^2$. We note that including the thermal dissipation term in the amplitude equation, $-BD_\delta\delta/2\delta_0$, alters slightly the most probable amplitude δ_m determined through $V'(\delta_m) = dV/d\delta|_{\delta_m} = -BD_\delta/2\delta_0 - \delta_m/\tau_\delta + {\delta_m}^{3/2}/\tau_\delta\delta_0^{1/2} = 0$. Consequently, the variance σ_δ^2 of $P(\delta)$ is modified. It is suggested in [20] that as long as the thermal dissipation term is involved in the LSC amplitude equation, Ro-dependent coefficients are included in all fluid momentum terms, in order that $P(\delta_0)$ is maximum and σ_δ^2 is invariant. Nevertheless, the physical origin of these coefficients is not well understood. We find that including the thermal dissipation term in our model does not change significantly the potential barrier $\Delta V = V(0) - V(\delta_m)$. Hence it does not influence much the occurrence frequency and other dynamical properties of cessations. For these reasons we have retained the amplitude equation in its present format.

The results of $P(\delta/\delta_0)$ are shown in Fig. 4(a) for several Ro. When Ro $\gtrsim 5$ the data of $P(\delta/\delta_0)$ collapse into one single curve. In this range the Coriolis force is so weak that it has not yet altered the LSC strength δ_0 [Fig. 4(b)], thus the variance of $P(\delta/\delta_0)$ remains constant. When Ro $\lesssim 5$, the half-width of the PDF starts to increase gradually with decreasing Ro. In this range δ_0 decreases rapidly, indicating the decay of the LSC strength in the background of strong rotations [10,11]. We determine the parameters B, D_δ, and τ_δ in Eq. (4) as functions of Ro through theoretical fittings of $P(\delta/\delta_0)$ to the experimental data and compute the cessation frequency f_c. Since $\Delta V/D_\delta > 1$, we apply the large-barrier approximation and evaluate the first-passage time for $\delta(t)$ to reach $\tilde{\delta} \ll \delta_0$, using the Arrhenius formula

$$T(\tilde{\delta}) = \frac{\sqrt{2\pi D_\delta \tau_\delta}}{|V'(\tilde{\delta})|} \exp\left(\frac{2[V(\tilde{\delta}) - V(\delta_0)]}{D_\delta}\right). \tag{7}$$

Here $\tilde{\delta}$ is the minimum LSC amplitude during each cessation event. Experimental data reveal that $\tilde{\delta}$ has a nonuniform distribution $P_m(\tilde{\delta})$ in the range $0 \leqslant \tilde{\delta} \leqslant \delta_c$ that can be approximated as an exponential function $P_m(\tilde{\delta}) = P_m(0)e^{\eta\tilde{\delta}}$. Thus the cessation frequency can be determined when $T(\tilde{\delta})$ is averaged over zero to the threshold of cessation δ_c:

$$f_c = \frac{\delta_c}{\int_0^{\delta_c} T(\tilde{\delta}) P_m(\tilde{\delta}) d\tilde{\delta}}. \tag{8}$$

We find that results for f_c are mostly sensitive to the potential barrier $\Delta V \approx \delta_0^2/10\tau_\delta + BD_\delta/2 \approx \delta_0^2/10\tau_\delta$. The close agreement between the theoretical and experimental results of f_c shown in Fig. 4(c) implies that the observed Ro dependence of f_c can be well predicted by Eq. (4).

Also of interest is the mean angular change $\Delta\theta_c$ of the LSC during cessations [Fig. 2(b)]. We estimate the displacement $\Delta\theta_d$ due to diffusion of $\theta(t)$ within a mean cessation duration $\Delta\tau$. Based on the diffusivity $D_\theta(\delta)$ determined above (Fig. 3), we estimate the azimuthal displacement $\Delta\theta_d$ due to diffusive motion of $\theta(t)$ within the mean cessation duration $\Delta\tau$:

$$\Delta\theta_d = \left[\int_{-\Delta\tau/2}^{\Delta\tau/2} D_\theta(\delta) dt\right]^{1/2} = \left[2\int_{\tilde{\delta}}^{\delta_c} \frac{D_\theta(\delta) d\delta}{|\dot{\delta}|}\right]^{1/2}. \tag{9}$$

Here we have changed the integration variable using $dt = |\dot{\delta}|^{-1} d\delta$. During cessations when $\delta \ll \delta_0$, we observe that $\delta(t)$ varies linearly in time with a change rate given by the slope of $V(\delta)$ near $\delta = 0$: $|\dot{\delta}| = dV/d\delta|_{\delta \ll \delta_0} = BD_\delta/2\delta_0$. Substituting $D_\theta(\delta) = D_0\delta^{-2}$ obtained earlier, we arrive at

$$\Delta\theta_d = 2\left[\int_{\tilde{\delta}}^{\delta_c} \frac{D_0\delta_0}{BD_\delta\delta^2} d\delta\right]^{1/2}. \tag{10}$$

The results of $\Delta\theta_d$ for Ro $= 236$ are shown by the dashed line in Fig. 4(d) and compared with the experimental data of $\Delta\theta_c$. We see that when Ro > 70, the angular change during cessations are mainly determined by diffusive motion $\Delta\theta_c \approx \Delta\theta_d$. However, when Ro $\leqslant 70$, $\Delta\theta_c$ becomes larger than $\Delta\theta_d$ because the mean drift velocity of $\langle\dot{\theta}\rangle$ due to the Coriolis force starts to exceed $\Delta\theta_d/\Delta\tau$.

The angular displacement $\Delta\theta_c$ has a preference in the retrograde direction. We count the number of the cessation events N_+ (N_-) if the net displacement $\Delta\theta_c$ is in the prograde (retrograde) direction. The ratio of N_+/N_- is depicted in Fig. 4(e) as a function of Ro. We see that $N_+/N_- \approx 0.6 \pm 0.1$ when Ro $\geqslant 70$, but decreases with decreasing Ro. The underlying mechanism for the observed directional azimuthal displacements during cessations is not well understood. We infer that it is associated with the gradual variation in δ when cessations occur. As predicted by Eq. (4), during cessations the change rate $|\dot{\delta}| = dV/d\delta|_{\delta\approx 0} = BD_\delta/2\delta_0$ remains finite and independent of δ [23,24].

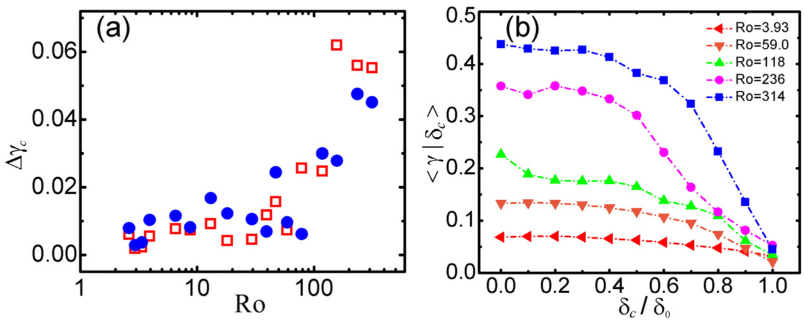

FIG. 5. (a) Enhanced ratio $\Delta\gamma_c$ due to cessations. Open squares show experimental data and closed circles the theoretical estimate of $\Delta\gamma_c$. (b) Conditional mean of $\langle\gamma|\delta_c\rangle$ as a function of δ_c/δ_0. Results were obtained using time series of $\theta(t)$ with $\delta \geqslant \delta_c$.

The traces of $\delta(t)$ exhibit a wedge shape as shown in Fig. 2(b). Thus the LSC retains substantial strength. The fluid momentum produced by the Coriolis force, $\delta\Omega/\tau_{\dot\theta}\delta_0$, continues to accelerate the LSC rotations preferentially in the retrograde direction.

D. Enhanced rotation speed ratio due to cessations

Our interpretation for the observed increasing rotation speed ratio γ in a large-Ro range is as follows. When small-amplitude events (such as cessations) occur, the inertial damping for the LSC azimuthal motion decreases. The diffusivity of θ, $D_\theta = D_0\delta^{-2}$, increases accordingly and gives rise to large azimuthal velocities $\dot\theta$. The dynamical properties of cessations, including the occurrence frequency f_c and the angular displacement $\Delta\theta_c$, are however independent of Ro when Ro $\geqslant 5$, since the Coriolis force has not yet altered the LSC strength δ under weak rotations [Figs. 4(b)–4(d)]. Thus, with increasing Ro, the angular displacements during cessations take a larger part in the LSC azimuthal motion and increase $\langle\dot\theta\rangle$ further. An increase in γ should occur when the enhanced $\langle\dot\theta\rangle$ due to cessations exceeds the mean drift velocity ascribed to the Coriolis force along. The cessation-enhanced γ can be estimated based on the measured properties: $\Delta\gamma_c = f_c\Delta\theta_c(N_- - N_+)/(N_- + N_+)\Omega$. Our theoretical estimate of $\Delta\gamma_c$ is compared with the experimental results in Fig. 5(a). They imply that $\Delta\gamma_c$ is insignificant with small Ro, but becomes important when Ro > 70.

To clarify how the mean azimuthal rotation speed is dependent on δ for various Ro, we show in Fig. 5(b) the conditional mean $\langle\gamma|\delta_c\rangle$, determined by time series of $\theta(t)$ with all small-amplitude events ($\delta < \delta_c$) removed (as explained in detail in Appendix C). We find that $\langle\gamma|\delta_c\rangle$ decreases with increasing δ_c. The reduction in γ is greater with a larger Ro. The different curves of $\langle\gamma|\delta_c\rangle$ for various Ro appear to converge to a low value of 0.06 ± 0.02 when $\delta_c \approx \delta_0$. We find that the reduction of γ when removing the cessation events, $\Delta\gamma = \langle\gamma|0\rangle - \langle\gamma|\delta_c\rangle$, is in agreement with our estimate as shown in Fig. 5(a).

E. Prediction of the turbulent viscosity coefficient

To account for the observed nontrivial Ro dependence of the LSC retrograde rotation velocity (Fig. 1), whose value is much lower than that predicted by theory [13], we suggest that an additional viscous damping term $f_K = -K(\delta)\dot\theta/\tau_{\dot\theta}$ is involved in the LSC orientation equation

$$\ddot\theta = -\frac{1}{\tau_{\dot\theta}}\left(\frac{\delta}{\delta_0} + K\right)\dot\theta + \frac{\delta\Omega}{\delta_0\tau_{\dot\theta}} + f_{\dot\theta}(t). \quad (11)$$

Such a greater level of viscous damping has been attributed to turbulent viscosity before [11,12]. We propose here that f_K is sensitive to the LSC strength δ. The coefficient K can be determined

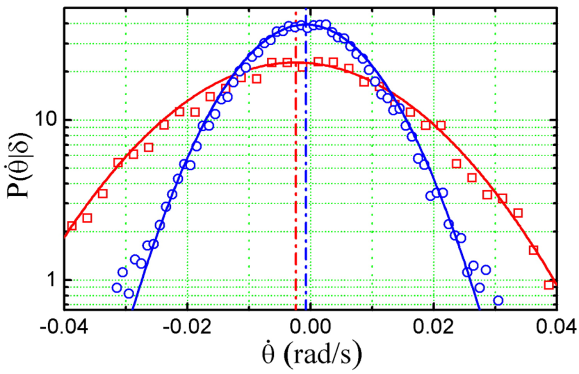

FIG. 6. Conditional probability distributions $P(\dot{\theta}|\delta)$ for given amplitudes δ with Ro = 236. Red squares show $\delta = 0.3\delta_0$ and blue circles $\delta = 0.5\delta_0$. The solid curves are theoretical fittings of $P(\dot{\theta}|\delta)$ based on Eq. (12). The two vertical dash-dotted lines indicate the axis of symmetry of $P(\dot{\theta}|\delta)$.

through theoretical fittings of the conditional PDF $P(\dot{\theta}|\delta)$ to the experimental data. Previous works [19,23] considered the complete PDF $P(\dot{\theta})$ with all values of the LSC amplitude δ associated and found that the PDF undergoes a transition from a large-amplitude regime ($\delta \geqslant \delta_0$) where $P(\dot{\theta})$ is Gaussian to a small-amplitude regime ($\delta \leqslant \delta_0$) where $P(\dot{\theta})$ becomes a power function. In Eq. (11) the effect of turbulence stress on the LSC azimuthal motion is modeled by an additional viscous damping f_K that is independent of the inertia damping. Since $\tau_{\dot{\theta}} \ll \tau_\delta$, we consider this equation as a Langevin equation of $\dot{\theta}$ with coefficients dependent on δ and determine the steady-state conditional PDF $P(\dot{\theta}|\delta)$ for a given value of δ:

$$P(\dot{\theta}|\delta) = C \exp\left[- \left(K + \frac{\delta}{\delta_0} \right) \left(\dot{\theta} - \frac{\Omega}{1 + K\frac{\delta_0}{\delta}} \right)^2 \Big/ \tau_{\dot{\theta}} D_{\dot{\theta}} \right], \tag{12}$$

with C a normalization constant. Thus $P(\dot{\theta}|\delta)$ is a Gaussian distribution, with the most probable azimuthal velocity $\dot{\theta}_m$ given by

$$\dot{\theta}_m = \Omega/(1 + K\delta_0/\delta). \tag{13}$$

We measured the instantaneous azimuthal velocity $\dot{\theta}$ and determined the conditional PDF $P(\dot{\theta}|\delta)$ with δ restricted in the range of $(\delta - 0.1\delta_0, \delta + 0.1\delta_0)$. Experimental results reveal that distributions of $P(\dot{\theta}|\delta)$ for all δ indeed have a Gaussian shape. In Fig. 6 we compare two sets of data of $P(\dot{\theta}|\delta)$ with $\delta = 0.3\delta_0$ and $0.5\delta_0$, respectively. One can see that with a smaller LSC amplitude δ the variance of $P(\dot{\theta}|\delta)$ increases and the axis of symmetry shifts further to the left. We determine the axis of symmetry of $P(\dot{\theta}|\delta)$, $\dot{\theta} = \dot{\theta}_m$, through theoretical fitting of Eq. (12) to the experimental data. Results for the turbulent viscosity coefficient K are then obtained through Eq. (13).

Figure 7(a) shows that results of $K(\delta)$ for a constant rotating rate (Ro = 236). One can see that with increasing δ, $K(\delta)$ increases and is approximately a power function: $K \sim \delta^\eta$ with $\eta \approx 4$. Although such a power-law dependence of K on δ is not well understood, it suggests that during cessation events when the LSC flow strength decreases, the fluctuation of the fluid velocity decreases significantly. When $\delta < 0.5\delta_0$ and $K(\delta) \ll 1$, the turbulent viscous effect is negligible. Equation (11) suggests that the diffusivity of $\dot{\theta}$ is then mainly given by the inertial damping and follows $D_{\theta}(\delta) = \Gamma_\theta \tau_{\dot{\theta}}^2 \delta_0^2 \delta^{-2}$. When the LSC amplitude δ is at its mean δ_0, $K = 5.6$ far exceeds one and we find $\gamma(\delta = \delta_0) = \dot{\theta}_m/\Omega = 1/(1 + K) \approx 1.5$, in agreement with our observations in the range of Ro $\leqslant 70$ where the enhancement of γ due to cessations is negligible [Fig. 5(a)]. For $\delta > \delta_0$ the turbulence stress is one order of magnitude larger than the inertial damping, leading to a significant reduction of the LSC azimuthal rotation velocity, as evident in Fig. 5(b).

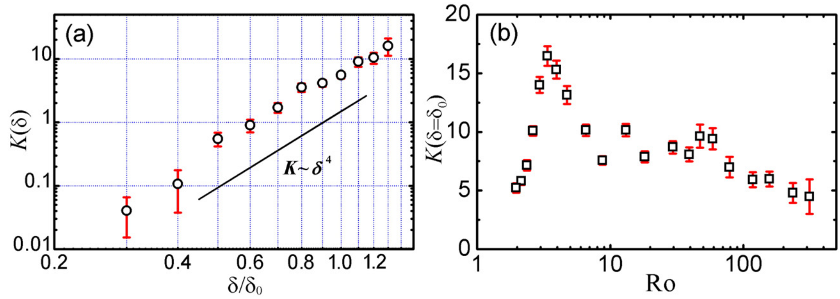

FIG. 7. (a) Turbulent viscosity coefficient K as a function of δ with $\mathrm{Ro} = 236$. The solid line indicates a power function of $K \sim \delta^4$. (b) $K(\delta = \delta_0)$ as a function of Ro. The standard deviations in determining K mainly come from the uncertainty when fitting the experimental data of $P(\dot{\theta}|\delta)$ with the Gaussian function (12), indicated by the error bars.

In Fig. 7(b) we show results for $K(\mathrm{Ro})$ when $\delta = \delta_0$ for each Ro. One can see that in the slow rotation range ($\mathrm{Ro} \geqslant 5$) where δ_0 is independent of Ro [Fig. 4(b)], K increases with decreasing Ro, suggesting that the magnitude of the turbulent stress is larger when the rotating velocity of the sample increases. In the range of $1 \lesssim \mathrm{Ro} \leqslant 5$, K varies rapidly as a function of Ro and reaches a maximum at $\mathrm{Ro} = 3.4$. The variations of $K(\mathrm{Ro})$ in this range can be preliminarily understood by the Ro dependence of the LSC strength δ_0 depicted in Fig. 4(b).

IV. CONCLUSION

In this paper we reported persistent retrograde rotation of the LSC in turbulent rotating RBC within a large Ro number range $1 \lesssim \mathrm{Ro} \leqslant 314$. The rotation speed ratio γ first experiences a complicated Ro dependence of γ in the range $1 \leqslant \mathrm{Ro} \lesssim 10$ that agrees with previous works [11,12]. In the range of $10 \lesssim \mathrm{Ro} \leqslant 70$, γ remains a constant of 0.13 ± 0.01 independent of Ro. When $\mathrm{Ro} \geqslant 70$, γ gradually increases with increasing Ro and reaches a value of 0.42 for $\mathrm{Ro} = 314$.

The enhanced azimuthal rotation velocity of the LSC in the large-Ro range is largely ascribed to the fluctuations of its circulating strength during small-amplitude events (cessations). When cessation occurs, the LSC rotational inertia decreases and its circulating plane moves more freely in the azimuthal direction. It was found that the azimuthal motion of the LSC is characterized by normal diffusion in the background of linear retrograde rotation. The diffusivity of $\theta(t)$ follows closely a simple power function $D_\theta(\delta) = D_0\delta^{-2}$. The conditional mean of the instantaneous azimuthal velocities is given by $\langle|\dot{\theta}|_\delta\rangle = \dot{\theta}_0(\delta/\delta_0)^{-1.16}$. Both observations are interpreted by the equation of motion for $\theta(t)$ [Eq. (1)].

The stochastic phenomenon of cessations (and the general small-amplitude events) under weak rotations can be well predicted through the LSC amplitude equation (4). We determined the parameters in this equation through theoretical fittings of $P(\delta/\delta_0)$ to the experimental data and determined the cessation frequency f_c. The theoretical prediction was shown to be in good agreement with the experiment. The cessation frequency f_c and the magnitude of angular displacement $\Delta\theta_c$ during cessations were found to be independent of Ro in the large-Ro range. With the measured dynamical properties of cessation events we further deduced the enhancement of the LSC rotation speed ratio $\Delta\gamma_c$ that is found to agree with the experimental results. Further, $\Delta\gamma_c$ is insignificant for small Ro, but increases and becomes important when $\mathrm{Ro} > 70$.

In order to explain the Ro dependence of the LSC retrograde rotation velocity, whose value is much lower than the theoretical prediction (Fig. 1), we introduced an additional turbulent viscous damping term in the LSC orientation equation (11). The turbulent viscosity coefficient $K(\delta)$, determined through the conditional PDF of the instantaneous LSC azimuthal velocity, was found to increase sensitively with increasing δ. In the slow-rotation range ($\mathrm{Ro} \leqslant 5$), K increases with decreasing

Ro, indicating that the LSC experiences a stronger turbulent stress when the sample rotating speed increases. In the fast-rotation range of $1 \lesssim \mathrm{Ro} \leqslant 5$, K varies rapidly as a function of Ro and reaches a maximum at $\mathrm{Ro} = 3.4$. We suggested that the variation of $K(\mathrm{Ro})$ in this range is relevant to the Ro dependence of the mean LSC strength δ_0, which interprets the nontrivial Ro dependence of the LSC retrograde rotation speed ratio $\gamma(\mathrm{Ro})$.

ACKNOWLEDGMENTS

We are grateful to K.-Q. Xia, J. Aurnou, R. P. J. Kunnen, S.-D. Huang and S. Sterl for helpful comments. This work was supported by the National Science Foundation of China through Grant No. 11572230 and a NSFC/RGC Joint Research Grant No. 11561161004.

APPENDIX A: PROBABILITY DISTRIBUTION OF THE LSC ORIENTATION

Experimental observation of the probability distribution of the LSC orientation suggests that the small thermal inhomogeneity over the top plate (discussed in Sec. II) still produces a biased azimuthal orientation. Figure 8 shows $P(\theta_r)$ for two Ro numbers with θ_r the reduced LSC orientation modulo 2π $(0 \leqslant \theta_r \leqslant 2\pi)$. With a very slow rotating rate ($\mathrm{Ro} = 236$) we notice a maximum of $P(\theta_r) = 2.5$ close to the coldest angular position of the top plate. This asymmetry effect may to some extent affect the azimuthal dynamics of the LSC. Nevertheless, the magnitude of the maximum in $P(\theta_r)$ is comparable to nonrotating experimental results reported elsewhere [13]. Moreover, we find that the influence of the LSC azimuthal rotation due to such an asymmetry is milder and becomes insignificant when a large Ω is applied. As shown in Fig. 8, $P(\theta_r)$ is more uniformly distributed for $\mathrm{Ro} = 2.2$. We have made no attempt to compensate this asymmetry by tilting the cell to produce additional buoyancy force that may balance the asymmetric cooling of the top plate as suggested in [13], with the objective of maintaining the direction of Ω precisely parallel to the gravity.

It is suggested that the earth's Coriolis force creates a potential well for the LSC azimuthal diffusion [13], $V_E(\theta) = A_E\cos(\theta) + B_E\theta$, with $A_E = 2a\Omega_E\cos(\phi)/(1 + 12\,\mathrm{Re}^{-0.5})$ and $B_E = \Omega_E\sin(\phi)/(1 + 12\,\mathrm{Re}^{-0.5})$. Here ϕ is the latitude and a is a constant of order one that reveals the ratio of the Coriolis force applied to horizontal and vertical flows. With strong background turbulent fluctuations $V_E(\theta)$ does not affect the net rotation rate $\langle\dot{\theta}\rangle$ [13]; however, it produces a preferred orientation at $\theta = \theta_m$ where $dV_E(\theta)/d\theta|_{\theta=\theta_m} = 0$. When deliberate rotations are applied, the potential well for θ becomes $V(\theta) = A\cos(\theta) + B\theta$, where $A = 2a\Omega_E\cos(\phi)/(1 + 12\,\mathrm{Re}^{-0.5})$ and $B = [\Omega + \Omega_E\sin(\phi)]/(1 + 12\,\mathrm{Re}^{-0.5})$. The potential barrier disappears if $\Omega \geqslant 2a\Omega_E\cos(\phi)$. Since in the experiment $\Omega \geqslant 10\Omega_E$, we do not observe any correlation of the maximum in $P(\theta_r)$ and the preferred orientation θ_m due to the earth's Coriolis force.

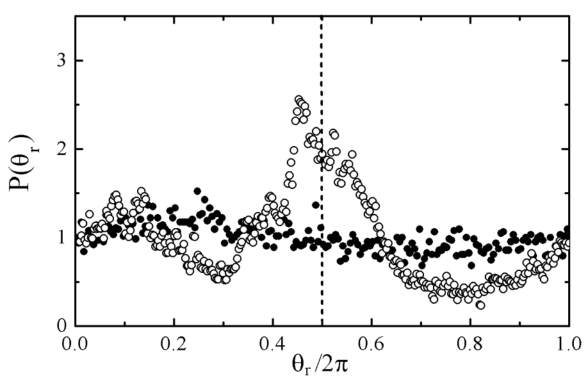

FIG. 8. Probability distribution of the reduced orientation $P(\theta_r)$ for $\mathrm{Ro} = 236$ (open symbols) and $\mathrm{Ro} = 2.2$ (closed symbols). The dashed line indicates the orientation of the inlet of the coolant channel in the top plate.

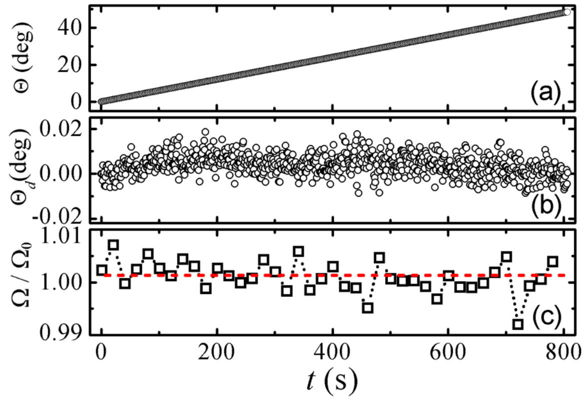

FIG. 9. (a) Time series of $\Theta(t)$ for a preconcerted sample rotating rate $\Omega_0 = 1.05 \times 10^{-3}$ rad/s. (b) Detrended orientation of the sample $\Theta_d(t)$. (c) Results for $\Omega(t)/\Omega_0$. Here $\Omega(t)$ is determined by the mean slope of $\Theta(t)$ in every 20 s. The dashed line indicates $\langle\Omega(t)\rangle = 1.0013\Omega_0$.

APPENDIX B: MEASUREMENTS OF THE ROTATING VELOCITY OF THE SAMPLE $\Omega(t)$

The convection sample was mounted on a rotary table (Nikken, model CNC260) with high-quality performance for slow-rotating experiments. The table had a carbide worm system with high indexing accuracy and gave smooth and jerk-free motion when Ω covered the range $7.85 \times 10^{-4} \leqslant \Omega \leqslant 0.1$ rad/s. To measure the mean sample rotating speed Ω and its fluctuations in time, we took pictures of the table with a position mark on it. The azimuthal orientation of the mark $\Theta(t)$ was then recorded. Figure 9(a) shows $\Theta(t)$ for the run with a preconcerted rotating speed $\Omega_0 = 1.05 \times 10^{-3}$ rad/s. The fluctuation of $\Theta(t)$ from its prescribed linear trend is shown in Fig. 9(b) by the detrended orientation: $\Theta_d(t) = \Theta(t) - \Omega_0 t$. Figure 9(c) shows the result of $\Omega(t)/\Omega_0$ derived from $\Theta(t)$. We find that the mean value of $\Omega(t)$ (dashed line) is slightly greater than Ω_0. Over the whole sampling period, the deviation of $\Omega(t)$ from Ω_0 and the rms fluctuation in $\Omega(t)$ are both within 1%.

APPENDIX C: CONSTRUCTION OF TIME SERIES $\theta(t)$ WITH LARGE AND SMALL LSC AMPLITUDES

The procedure is illustrated in Figs. 10(a)–10(c). The original time series $\theta(t)$ for Ro = 236 is shown by the solid line in Fig. 10(a), which contains one cessation event ($\delta < 0.5\delta_0$) indicated in red. By shifting the data points along the two axes, we remove the section of cessation and link the two portions of large amplitude ($\delta \geqslant 0.5\delta_0$) together. The modified time series with large amplitude is shown by the blue dashed line. Similarly, sections in $\theta(t)$ with large amplitude are removed to construct time series of small amplitude as shown in Fig. 10(b). We thus obtain $\theta(t)$ with large (small) amplitude shown by the blue (red) line in Fig. 10(c). It can be seen that the small-amplitude time series still reveals diffusive meandering motion, with a mean drift velocity much larger than $\langle\dot{\theta}\rangle$ for the entire data set with this Ro.

It was commonly assumed that cessation events, normally defined by a relatively small threshold of δ_c, were rare and the contribution of angular displacements during cessations to the net azimuthal rotation of the LSC flow was ignored [10,11,13]. However, both our experimental data and theoretical model show that the probability distribution function $P(\delta)$ increases exponentially with increasing δ in the small-amplitude regime. This result implies that the number of cessation events, or small-amplitude events in general, would increase rapidly if the threshold value of the events δ_c is increased. Thus the angular displacement of the small-amplitude event would become important.

We consider the cumulative angular displacement of all the small-amplitude events [for example, displacement of the red curve in Fig. 10(c)] $\Delta\theta_{\delta<\delta_c}$ and the time duration $\Delta T_{\delta<\delta_c}$. The ratio of

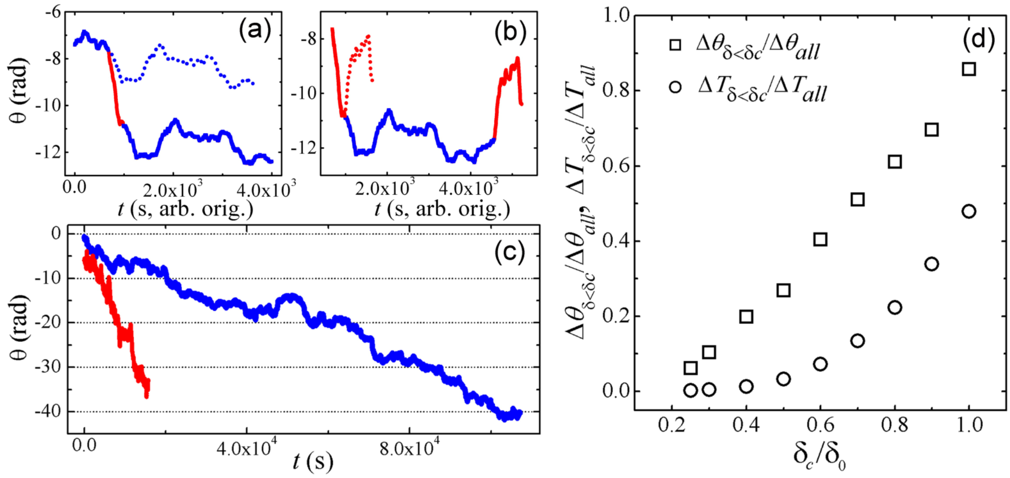

FIG. 10. Time series of $\theta(t)$ for Ro $= 236$. Sections in $\theta(t)$ with δ greater (smaller) than $\delta_c = 0.5\delta$ are shown in blue (red). (a) Example of removing an event with small amplitude in $\theta(t)$. (b) Example of removing an event with large amplitude. (c) Resulting long time series of large and small amplitude. For clarity of demonstration we show here a small-amplitude time series (red curve) extracted from experimental data of 100 h, with the initial orientation shifted by 5 rad apart from zero. The large-amplitude time series (blue curve) is obtained from experimental data over 30 h. (d) Ratios of the angular displacement $\Delta\theta_{\delta<\delta_c}/\Delta\theta_{\rm all}$ and time duration $\Delta T_{\delta<\delta_c}/\Delta T_{\rm all}$ as functions of the cessation threshold δ_c/δ_0.

$\Delta\theta_{\delta<\delta_c}/\Delta\theta_{\rm all}$ and $\Delta T_{\delta<\delta_c}/\Delta T_{\rm all}$ are shown in Fig. 10(d) as a function of δ_c/δ_0 for Ro $= 236$. Here $\Delta\theta_{\rm all}$ and $\Delta T_{\rm all}$ are the angular and time span of the entire data set of $\theta(t)$. It appears that both $\Delta\theta_{\delta<\delta_c}$ and $\Delta T_{\delta<\delta_c}$ increase with increasing δ_c. The time duration $\Delta T_{\delta<\delta_c}$ appears to follow a more sensitive dependence on the threshold value δ_c. One remarkable observation in Fig. 10(d) is that the time series of $\theta(t)$ with $\delta < \delta_0$ has taken up a fraction of 86% in the entire azimuthal displacement $\Delta\theta_{\rm all}$.

---

[1] G. K. Vallis, *Atmospheric and Oceanic Fluid Dynamics* (Cambridge University Press, Cambridge, 2006), p. 745.

[2] J. Marshall and F. Schott, Open-ocean convection: Observations, theory and models, Rev. Geophys. **37**, 1 (1999).

[3] R. S. Lindzen and A. Y. Hou, Hadley circulation for zonally averaged heating centered off the equator, J. Atmos. Sci. **45**, 2416 (1988).

[4] G. Ahlers, S. Grossmann, and D. Lohse, Heat transfer and large scale dynamics in turbulent Rayleigh-Bénard convection, Rev. Mod. Phys. **81**, 503 (2009).

[5] D. Lohse and K.-Q. Xia, Small-scale properties of turbulent Rayleigh-Bénard convection, Annu. Rev. Fluid Mech. **42**, 335 (2010).

[6] R. Krishnamurti and L. N. Howard, Large scale flow generation in turbulent convection, Proc. Natl. Acad. Sci. USA **78**, 1981 (1981).

[7] J. J. Niemela, S. Babuin, and K. R. Sreenivasan, The wind in confined thermal convection, J. Fluid Mech. **449**, 169 (2001).

[8] E. Brown, A. Nikolaenko, and G. Ahlers, Reorientation of the Large-Scale Circulation in Turbulent Rayleigh-Bénard Convection, Phys. Rev. Lett. **95**, 084503 (2005).

[9] H.-D. Xi, S.-Q. Zhou, Q. Zhou, T.-S. Chan, and K.-Q. Xia, Origin of the Temperature Oscillation in Turbulent Thermal Convection, Phys. Rev. Lett. **102**, 044503 (2009).

[10] R. P. J. Kunnen, H. J. H. Clercx, and B. J. Geurts, Breakdown of large-scale circulation in turbulent rotating convection, Europhys. Lett. **84**, 24001 (2008). In plotting this data set in Fig. 1, data points with the two lowest Ro are removed because of the imminent breakdown of the LSC in this low-Ro regime. R. P. J. Kunnen (private communication).

[11] J.-Q. Zhong and G. Ahlers, Heat transport and the large-scale circulation in rotating turbulent Rayleigh-Bénard convection, J. Fluid Mech. **665**, 300 (2010).

[12] J. E. Hart, S. Kittelman, and D. R. Ohlsen, Mean flow precession and temperature probability density functions in turbulent rotating convection, Phys. Fluids **14**, 955 (2002).

[13] E. Brown and G. Ahlers, Effect of the Earth's Coriolis force on the large-scale circulation of turbulent Rayleigh-Bénard convection, Phys. Fluids **18**, 125108 (2006). The latitude $\phi = 34.46^\circ$ has been taken into account in determining $\gamma = \omega/(\Omega \sin\phi)$.

[14] C. Sun, H.-D. Xi, and K.-Q. Xia, Azimuthal Symmetry, Flow Dynamics, and Heat Transport in Turbulent Thermal Convection in a Cylinder with an Aspect Ratio of 0.5, Phys. Rev. Lett. **95**, 074502 (2005).

[15] J.-Q. Zhong, S. Sterl, and H.-M Li, Dynamics of the large-scale circulation in turbulent Rayleigh-Bénard convection with modulated rotation, J. Fluid Mech. **778**, R4 (2015).

[16] S. Sterl, H.-M Li, and J.-Q Zhong, Dynamical and statistical phenomena of circulation and heat transfer in periodically forced rotating turbulent Rayleigh-Bénard convection, Phys. Rev. Fluids **1**, 084401 (2016).

[17] H.-D. Xi, Q. Zhou, and K.-Q. Xia, Azimuthal motion of the mean wind in turbulent thermal convection, Phys. Rev. E **73**, 056312 (2006).

[18] E. Brown and G. Ahlers, Large-Scale Circulation Model for Turbulent Rayleigh-Bénard Convection, Phys. Rev. Lett. **98**, 134501 (2007).

[19] M. Assaf, L. Angheluta, and N. Goldenfeld, Rare Fluctuations and Large-Scale Circulation Cessations in Turbulent Convection, Phys. Rev. Lett. **107**, 044502 (2011).

[20] M. Assaf, L. Angheluta, and N. Goldenfeld, Effect of Weak Rotation on Large-Scale Circulation Cessations in Turbulent Convection, Phys. Rev. Lett. **109**, 074502 (2012).

[21] H. Risken, *The Fokker-Planck Equation: Methods of Solutions and Applications* (Springer, Berlin, 1996), p. 472.

[22] C. W. Gardiner, *Handbook of Stochastic Methods* (Springer, Berlin, 2004).

[23] E. Brown and G. Ahlers, A model of diffusion in a potential well for the dynamics of the large-scale circulation in turbulent Rayleigh-Bénard convection, Phys. Fluids **20**, 075101 (2008).

[24] E. Brown and G. Ahlers, Rotations and cessations of the large-scale circulation in turbulent Rayleigh-Bénard convection, J. Fluid Mech. **568**, 351 (2006).